Journal of ELECTRONIC MATERIALS, Vol. 47, No. 9, 2018
https://doi.org/10.1007/s11664-018-6420-5

Structural, Magnetic and Microwave Properties of Gadolinium-Substituted Ca-Ba M-Type Hexagonal Ferrites

M. KANWAL,[1,2,3] I. AHMAD,[1] T. MEYDAN,[2] J.A. CUENCA,[2] P.I. WILLIAMS,[2] M.T. FARID,[1] and G. MURTAZA[1]

1.—Department of Physics, Bahauddin Zakariya University, Multan 60800, Pakistan. 2.—Wolfson Centre of Magnetics, Cardiff School of Engineering, Cardiff University, Cardiff, Wales, UK. 3.—e-mail: muddassara@bzu.edu.pk

This paper presents a study on attempting to substitute Gd into a Ca-Ba M-type hexaferrite ($Ca_{0.5}Ba_{0.5}Gd_xFe_{12-x}O_{19}$, where x = 0, 0.05, 0.1, 0.15, 0.2, 0.25) using the sol–gel method. The structural, magnetic and microwave properties of the resultant material were investigated. Since Gd has a much larger ionic radius than Fe, substitution is not straightforward as revealed by the structural analysis. X-ray diffraction (XRD) patterns revealed some substitution into the M-type phase due to a changing lattice parameter; however, significant quantities of additional phases of hematite (α-Fe_2O_3) and gadolinium orthoferrite started to form at concentrations of up to Gd = 0.10 and at higher Gd concentrations, respectively. High-resolution transmission electron microscopy of selected compositions showed d-spacings corresponding to the three phases observed in XRD, confirming the incomplete substitution of Gd. Scanning electron microscopy showed platelet-shaped grains. Vibrating sample magnetometry at room temperature showed varied results owing to a myriad of interactions from the hexaferrite and secondary phases. The microwave complex permittivity and permeability in the frequency range of 2–11 GHz showed little frequency dependence with nominal values for the complex permeability. All the compositions exhibit low magnetic losses with frequency except Gd = 0.10. Such type of materials can be used for microwave devices in the low-GHz range and as well as permanent magnets.

Key words: Ca-Ba hexaferrites, magnetic properties, sol–gel process, permeability, permittivity, rare-earth substitution

INTRODUCTION

Barium and strontium hexaferrites were discovered in the 1950s. Due to their magnetic properties and cost-effectiveness, they are used in various domestic and commercial applications such as permanent magnets, magnetic recording media, microwave devices, electromagnetic wave shielding coatings, electric motors, antennas and many others.[1–8] Researchers working with hexaferrites are exploring the substitution of various elements to enhance their properties. The addition and replacement of Me^{2+} ions (Me^{2+} = Ca^{2+}, Ba^{2+} and Pb^{2+}) in barium or strontium hexaferrites showed remarkable effects on their properties.[9–14] In particular, tuneable magnetic saturation (M_s), coercivity (H_c) and magneto-crystalline anisotropy (H_a) have been demonstrated which is important for magnetically tuneable signal processing, magnetic storage media and many other applications.[15–17]

The partial replacement of Ba^{2+} with Ca^{2+} ions in the M-type ferrite reduced M_s due to non-collinearity of the spin structure.[18] The addition of different rare-earth (RE) ions (Ce^{3+}, Gd^{3+}, Eu^{3+}, La^{3+}, Nd^{3+}, Sm^{3+}, Pr^{3+} and Y^{3+}) were also studied for M-type hexaferrites.[19–25] Litsardakis et al.[21] reported a high H_c in Gd-added BaM ferrites due to the

(Received February 15, 2018; accepted May 29, 2018; published online June 13, 2018)

presence of additional nonmagnetic secondary phases. A decrease in M_s was also observed when Gd and Nd were substituted into BaM ferrites.[24] Me^{3+} ions like Al^{3+} and Cr^{3+} were also substituted to BaM and PbM ferrites.[5,26] The combination of Me^{2+} and Me^{3+} ions such as in La-Co doping is known to have a beneficial effect on H_c as well as H_a.[27] Co-Gd substitution into BaM ferrites also showed an improved H_c due to a high H_a field and lower M_s.[20] The change in microstructure and its effect on the magnetic properties as well as the dielectric properties have also been discussed by many researchers. Overall, La-Co-substituted M-ferrites are reported to be particularly useful for permanent magnets.[28] The doping of different elements also affects the microwave complex permeability and permittivity, which is important for determining the applicability in various microwave devices such as circulators, isolators, phase-shifters, passive microwave components and absorbers.[5,29–35]

To the best of our knowledge, structural modifications and their effects on the magnetic and microwave properties of Gd-doped calcium-substituted Ba hexaferrites has not been reported yet. Since calcium is a more abundant element than barium and strontium and belongs to the same periodic table group, these ferrites will be more economically viable. Moreover, in this study, the sol–gel method is employed to prepare the samples while other researchers mentioned earlier in this paper used the ceramic route or co-precipitation method to prepare hexagonal ferrites.[20,21] The sol–gel process produces a homogeneous product with particle size approaching the nano-sized range and also is cost-effective on a commercial scale. Since previously study has shown Gd to have some unusual magnetic properties when added in small amounts, Gd is doped to observe changes in magnetic properties; the optimal composition was observed when $x = 0.10$. It was also observed that Gd addition affects complex dielectric properties, but complex permeability remain unchanged.

EXPERIMENTAL

Chemicals

The chemicals used for the preparation of the $Ca_{0.5}Ba_{0.5}Gd_xFe_{12-x}O_{19}$ ($x = 0.0$–0.25) compositions were $Fe(NO_3)_3{\cdot}9H_2O$ (Sigma-Aldrich, 99%+), $Ba(NO_3)_2$ (Sigma-Aldrich, 99%+), $Gd(NO_3)_3$ (Sigma-Aldrich, 99%+) and $Ca(NO_3)_2$ (Sigma-Aldrich, 99%+) as precursors. NH_4OH solution (Analar, 34%) was used to maintain the pH while citric acid (Sigma-Aldrich, 99%+) was used as a chelating agent.

Synthesis

The Ca-Ba M-type hexaferrites (target phase: $Ca_{0.5}Ba_{0.5}Gd_xFe_{12-x}O_{19}$, where $x = 0.00$, 0.05, 0.10, 0.15, 0.20, 0.25) were prepared by the sol–gel method. The metal salt solutions for the required molarities were prepared in de-ionized water. The solutions were mixed and placed on a hot plate with a magnetic stirrer to homogenize the mixture. A stoichiometric amount of the citric acid was added as a chelating agent. The solution was evaporated slowly at 80°C with continuous stirring on the hot plate. After evaporation, the solution converted into a brown gel. The gel was then dried at 300°C for 2 h to obtain a powder. Finally, this powder was heat-treated at 900°C for 3 h in a carbolite furnace (type HTC 15/3) to obtain the required phase.

Characterization

X-ray diffraction (XRD) patterns of the samples were obtained using a Philips PW1710 x-ray diffractometer. Scanning electron microscopy (SEM) was performed using a Zeiss NTS S360 scanning electron microscope. High-resolution transmission electron microscopy (HRTEM), scanning tunneling electron microscopy (STEM) and energy-dispersive x-ray spectroscopy (EDX) of a selection of the samples was performed using a JEM-2100 electron microscope. The magnetic properties were measured using a Lakeshore vibrating sample magnetometer (VSM, model no. 7410) at room temperature. The effective complex permittivity ($\varepsilon_{r,eff} = \varepsilon'_{eff} - j\varepsilon''_{eff}$, where dielectric loss tangent is defined as $\tan\delta_\varepsilon = \varepsilon''_{eff}/\varepsilon'_{eff}$) and permeability ($\mu_{r,eff} = \mu'_{eff} - j\mu''_{eff}$, where magnetic loss tangent $\tan\delta_\mu = \mu''_{eff}/\mu'_{eff}$) of the powders were measured at discrete frequencies between 2 and 11 GHz using the cavity perturbation method[36–39] and a Keysight N5232 PNA-L microwave vector network analyser.

RESULTS AND DISCUSSION

X-ray Diffraction Analysis

The XRD patterns shown in Fig. 1a give the Gd doping and Fig. 1b reveals three separate phases; the M-type hexaferrite phase (ref no. 00-043-0002) and two secondary phases of hematite (α-Fe_2O_3, ref no. 00-024-0072) and gadolinium orthoferrite ($GdFeO_3$, ref no. 00-015-0196). Trace amounts of $GdFeO_3$ started to appear at Gd doping concentrations of greater than 0.1. The reason for the formation of these secondary phases is that Gd is only partially soluble into the M-type hexaferrite phase due to its large ionic radius, electronic configuration and magnetic moment.[40] Hence, the substitution of Gd may only occur up to a given threshold concentration, leading to the generation of the secondary phases.[21] Heat treatment and sintering temperatures affect the purity, where temperatures above 1000°C may obtain single phases with some compromise on grain size.[41,42] However, due to some laboratory limitations, this was not possible in the current study. Henceforth, all results presented are a bulk contribution of a multi-phase material. The averaged grain size of

each of the phases was calculated from XRD patterns using the Debye–Scherer formula. The calculated grain sizes lie in the nanometre range for all of the phases (from approximately 12 nm to 90 nm for the M-type hexaferrite phase, 16 nm to 87 nm for α-Fe_2O_3 and 10 nm to 65 nm for $GdFeO_3$). To specifically examine the concentration of Gd ions that substituted into the hexaferrite lattice, one can observe the (110) and (006) peaks at $2\theta \approx 30.3072°$ and $2\theta \approx 23.0839°$, respectively, associated with just the M-type hexaferrite. The lattice parameters '*a*' and '*c*' were calculated using the following equation:

$$d_{hkl} = \left(\frac{4}{3}\cdot\frac{h^2+hk+k^2}{a^2}+\frac{l^2}{c^2}\right)^{-\frac{1}{2}}$$

The calculated lattice parameter '*a*', shown in Fig. 2b, initially increases at concentrations below 0.05 and then decreases thereafter to its original value, while the lattice parameter '*c*' increases at Gd = 0.05, becomes constant at Gd = 0.1 and further increases at Gd = 0.25. The *c*/*a* ratio, shown in Fig. 2a, shows an increasing trend from 3.920 ±0.001 to 3.955 ±0.001 as the error calculated shows uncertainty in data up to three decimal points. This *c*/*a* ratio was well within agreement of already studied values of M-type structures; Verstegen and Stevels showed that M-type structures can be assumed if the observed *c*/*a* ratio value is less than 3.98.[43] The addition of Gd causes local distortion of the structure[44] which is represented in the change in *a* and *c* at low concentrations; however, at higher concentrations, the plateau response of *c* implies that addition of high-valence cations in the ferrites under an oxidizing environment introduces cation vacancies and dopant diffusion into M-type lattice is also affected.[45,46]

Gd substitution predominantly affects the '*a*' lattice parameter at low concentrations, and predominantly affects the '*c*' lattice parameter at higher concentration. The change in lattice parameters can be ascribed to dopant diffusion into the lattice, distortions in lattice due to ionic radii of dopants, creation of vacancies under oxidizing conditions and site occupancy.[45,46]

EDX measurements, obtained using STEM, are given in Table I and show the presence of different elements in the compositions. The wt.% values of Ba and Ca showed that Ca^{2+} is present along with Ba^{2+} ions in the barium M-type lattice.[21] The Gd wt.% value shows the presence of Gd-rich grains corresponding to Gd substituted into the M-type hexagonal lattice and $GdFeO_3$.[21,40] These results corroborate with those of XRD.

SEM Analysis

The SEM micrographs taken from a coarser grain area are given in Fig. 3. Figure 3a was taken at lower resolution of 500 μm to obtain a general view of the grain distribution. Figure 3b and c shows that the resultant material has pores as well as a grains and flaky structure. Ca and Gd have been shown to introduce porosity and flakiness in M-type hexagonal materials.[28,35,43] Park et al.[47] also observed platelet-shaped nano-grains in SrM ferrites.

HRTEM Analysis

The HRTEM image in Fig. 4a (x = 0.15) shows the morphology and grain distribution. A zoomed-in view of a selected coarser-grain area is given in Fig. 4b where x = 0.25 and the d-spacing corresponds to the (111) plane of $GdFeO_3$. Similarly, Fig. 4c and d, where x = 0.15, shows the d-spacing corresponding to the (114) plane of the M-type hexaferrite phase and the (104) plane of α-Fe_2O_3 (hematite phase), respectively. These images confirm the presence of the secondary phases identified in the XRD patterns. In Fig. 4d (x = 0.15), A represents the planes related to the grain and B represents the grain boundary.

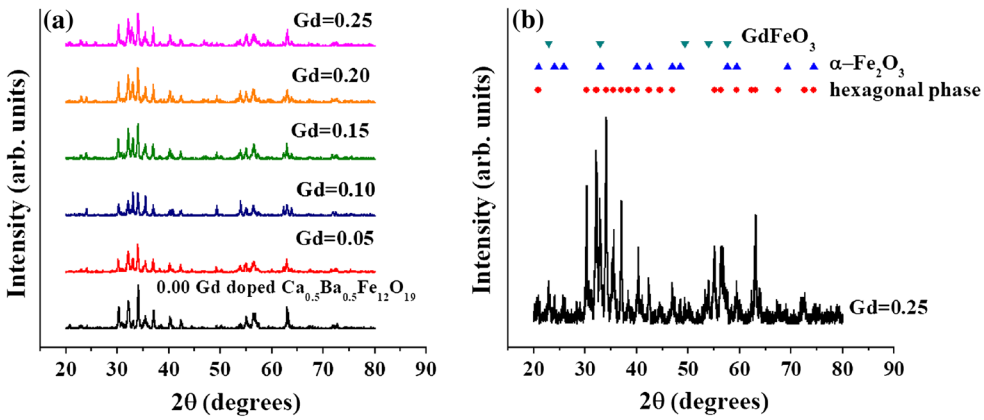

Fig. 1. (a) XRD patterns from 20° to 80° 2θ with varying Gd concentrations. (b) Pattern for Gd = 0.25 indicating three different phases: M-type hexaferrite, α-Fe_2O_3 and $GdFeO_3$.

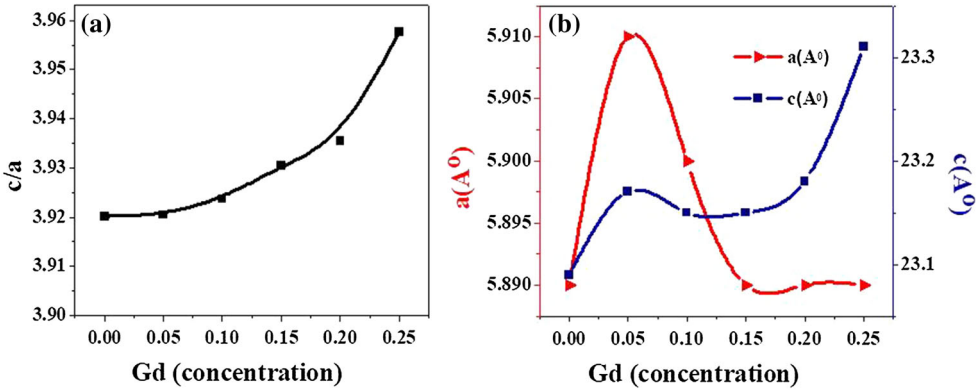

Fig. 2. Plot of (a) *c*/*a* ratio versus Gd concentration. (b) Calculated lattice parameters '*a*' and '*c*' versus Gd concentration from the XRD patterns of the M-type hexaferrite samples.

Table I. Data taken from EDX of STEM images of $Ca_{0.5}Ba_{0.5}Fe_{12-x}O_{19}Gd_x$

Gd (conc.)	O (wt.%)	Fe (wt.%)	Ca (wt.%)	Ba (wt.%)	Gd (wt.%)
x = 0.00	34.91–34.88	55.82–54.65	1.80–2.28	7.47–8.19	0
x = 0.15	41.65–22.48	48.11–65.17	2.92–1.67	4.47–7.08	2.85–3.61
x = 0.25	38.30–19.04	46.15–61.52	2.18–2.69	7.90–9.44	5.46–7.31

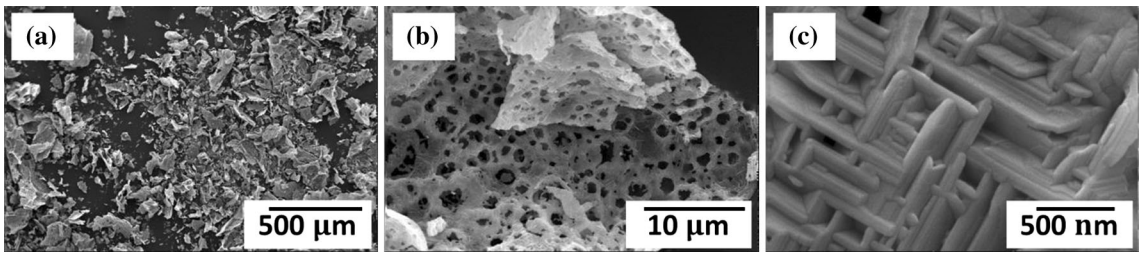

Fig. 3. Representative SEM micrographs taken from coarser-grain areas of Gd-doped Ca-Ba M-type hexaferrites: (a) low-resolution grain distribution, (b) selected area showing pores, and (c) platelet-shaped grain morphology.

Magnetic Properties

Room-temperature magnetic properties of the Gd-doped Ca-Ba M-type hexaferrites are shown in Fig. 5. M_s and H_a were calculated by using the law of approach to saturation magnetization[48–51] using the relation:

$$M = M_s\left(1 - \frac{A}{H} - \frac{B}{H^2}\right) + \chi H$$

where A is a constant which depends on microstress, inclusions and defects, B is a constant which arises due to the magneto-crystalline anisotropy and χH is the high-field susceptibility or forced magnetization. A is generally neglected at high magnetic fields and thus B can be calculated. The constant B can be calculated using the equation $B = Ha^2/15$ for a system with hexagonal symmetry.[32,52]

The variation of magnetic properties due to Gd doping is shown in Fig. 5, with values plotted in Fig. 6. It can be observed that M_s varies dramatically, with almost no correlation with Gd doping concentration. This is due to a myriad of factors including: the varying concentrations of the main hexaferrite phase and the secondary phases, the concentration of Gd that is actually substituted into the hexaferrite lattice and its effect on M_s of the intrinsic Ca-Ba M-type hexaferrite phase, the size and morphology of each of the phases and finally the packing density and geometrical variance in the sample preparation for each VSM measurement.

Addressing the contribution from each variable individually is not a trivial task since several mechanisms are present in each phase. The discussion henceforth gives a piecewise overview of magnetism within the M-type structure followed by the effects of the secondary phases.

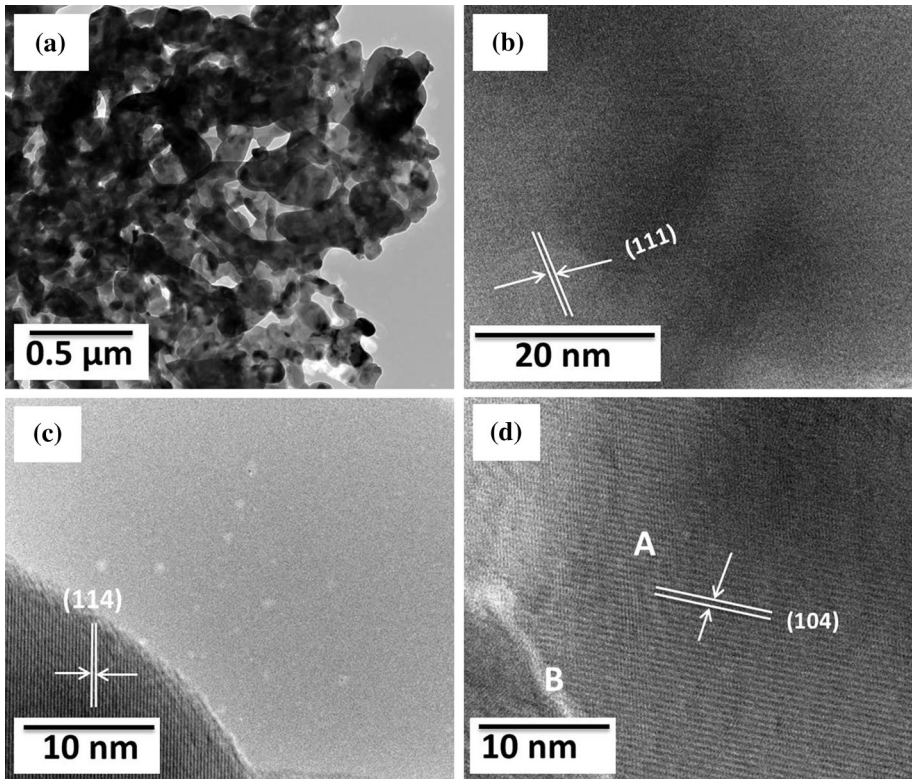

Fig. 4. Selected HRTEM micrographs of the Gd-doped Ca-Ba M-type hexaferrites: (a) the morphology of grain distribution for Gd = 0.15; (b) $GdFeO_3$ phase, d-spacing corresponding to the (111) plane for Gd = 0.25; (c) M-type hexaferrite phase, d-spacing corresponding to the (114) plane; and (d) Fe_2O_3 (hematite phase), d-spacing corresponding to (104) plane for Gd = 0.15. B shows grain boundaries and A shows planes of a grain.

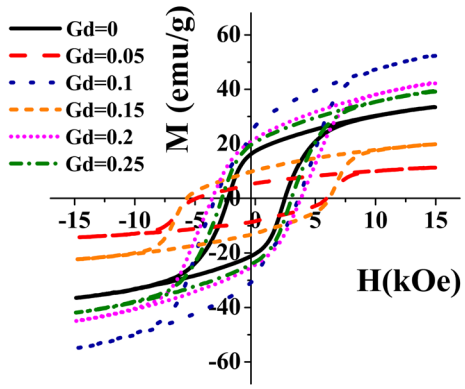

Fig. 5. M–H loops of $Ca_{0.5}Ba_{0.5}Fe_{12-x}O_{19}Gd_x$ (x = 0.00–0.25) at room temperature representing the magnetic behaviour of compositions at 15 kOe.

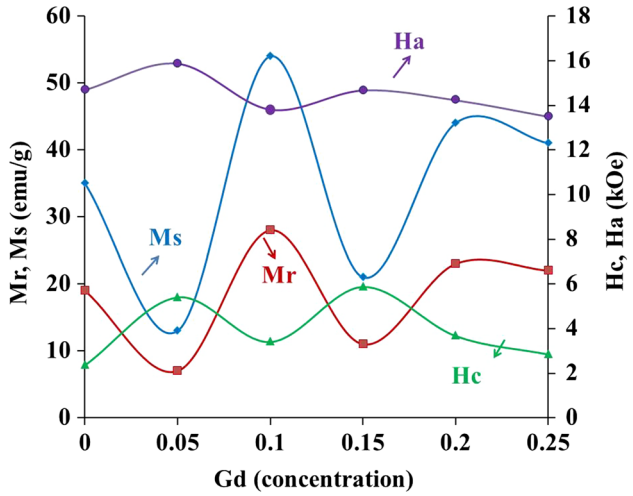

Fig. 6. Effect of Gd doping on H_a, H_c, M_s and M_r of the Ca-Ba M-type hexaferrite samples.

M-type hexaferrites contain Fe^{3+} ions in three types of coordination sites and five different crystallographic points. These coordination sites are octahedral, tetrahedral and trigonal bipyramid. The octahedral site is represented by 12k, 2a and 4f2, tetrahedral is represented by 4f1 and trigonal bipyramid is represented by 2b. Fe^{3+} ions with up-spin occupy 12k, 2a and 2b sites while opposite spins occupy 4f1 and 4f2 sites.[3,31] An explanation for the large variability in the magnetic properties may be explained by the influence of Gd doping concentration and impurity concentration on the spin states of these ions.

Decreases in M_s may be caused by magnetic dilution on the macroscopic and microscopic scale. On the microscopic scale, magnetic dilution occurs when Fe^{3+} (high spin) valence states change to a

low-spin Fe^{2+} (low spin) state at 2a sites. The Fe^{3+}–O–Fe^{3+} super exchange interaction is interrupted and weakened by Fe^{2+} ions and the phenomenon of spin canting may occur.[30,53] Another reason may be due to the presence of Ca influencing the Gd^{3+} substitution for Fe^{3+} ions which ultimately effects the (Gd, Fe)$^{3+}$–O–Fe^{3+}superexchange interaction in ferrites.[54] Substituted Gd also affects the hyperfine fields at 12k and 2b sites, which changes Fe^{3+}–O–Fe^{3+} superexchange interaction and hence net magnetization M_s.[30,55]

On the macroscopic scale, the ratio of hard-to-soft magnetic phases may also affect the magnetic properties.[56,57] The impurity phase of α-Fe_2O_3 has a low saturation magnetization and, therefore, with increasing concentration, will decrease the observed M_s.[58,59] Similarly, $GdFeO_3$ is antiferromagnetic at room temperature,[60] but there seems no correlation between the impurity phase concentration and M_s. Additionally, air gaps in the measured sample are due to the packing density of the sample powder; however, this systematic error is expected to be minimal as all samples are prepared by the same procedure.

H_c and H_a also vary inversely with M_s and M_r as can be seen in Fig. 6.[27] The interdependence of H_a and H_c is already a well-studied phenomenon.[27,30,32,55] Other parameters which affect the coercivity are particle size, composition and crystalline ordering.[54,55]

Microwave Permeability and Permittivity Properties

The effective microwave complex permittivity of the compositions $Ca_{0.5}Ba_{0.5}Gd_xFe_{12-x}O_{19}$ (x = 0.0–0.25) are shown in Fig. 7. The effective dielectric constant and losses shows a maximum at a Gd doping concentration of 0.10. An increase is noticed at approximately 8 GHz, but clear identification of this is not possible since the measurement is taken at discrete frequencies and is not continuous. Besides this increase, the dielectric constant is independent of frequency while the losses decrease with frequency which is typical of ferrites.[14,31] While an extremely sensitive technique, this is a limitation of the cavity perturbation method.

Dielectric properties in this frequency range can be ascribed to the polarization of Fe ions and atoms as well as any charge transfer mechanisms, i.e. electron hopping.[1] The addition of RE atoms (such as Gd) affects electron hopping mechanisms in the M-type hexaferrite lattice because their large ionic radii introduce defects and local strains.[59] In addition to the polarization mechanisms of the main hexaferrite phase, the additional secondary phases (α-Fe_2O_3 and $GdFeO_3$) create an inhomogeneous material with conducting and insulating inclusions. Polarization is therefore modelled using the Maxwell–Wagner–Sillars' model. Regions of the conducting phases are separated by the insulating phase, thereby effectively creating microscopic capacitors. On the application of an external electric field, charges in the conducting regions polarise at the insulating boundaries. Charge carriers, therefore, tend to accumulate at the grain boundaries and the observed result is a high resistance and dielectric constant.[60,61] Additionally, Koops theory states that when the frequency of the applied field is low, then polarisation is dominated by grain boundaries polarisation, whereas at higher frequencies, the polarisation mechanisms within the grains start to dominate.[62]

The effective complex permeabilities of the $Ca_{0.5}Ba_{0.5}Gd_xFe_{12-x}O_{19}$ (x = 0.0–0.25) compositions are shown in Fig. 8. Complex permeability in the microwave frequency range is normally associated with ferromagnetic resonance, whereby at frequencies higher than the natural resonance frequency, the magnetic permeability is equivalent to air. This resonance frequency is associated with H_a through:

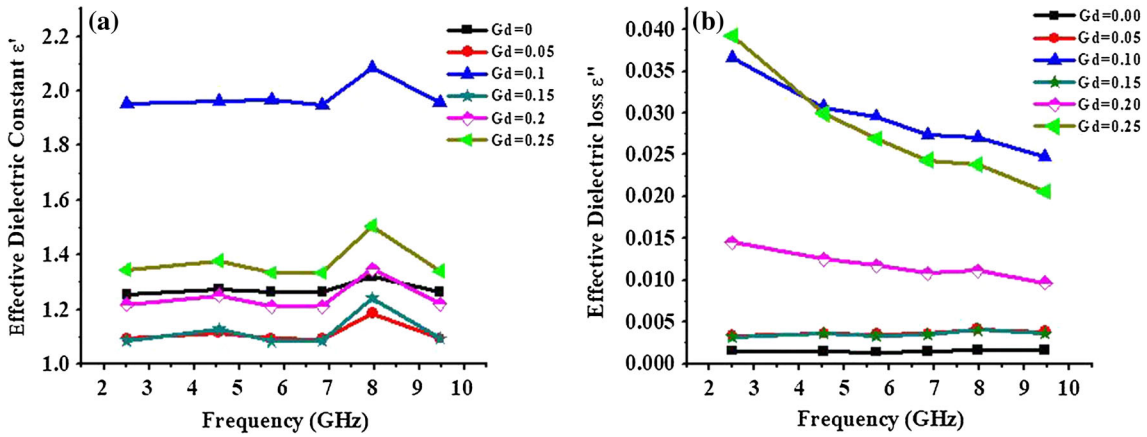

Fig. 7. Effective microwave complex permittivity of the Gd-doped Ca-Ba M-type hexaferrite samples using the cavity perturbation method. (a) The effective dielectric constant showed an increased at 8 GHz in all compositions. (b) The effective dielectric loss decreases with frequency, while the largest loss was obtained for Gd doping concentrations of 0.1 and 0.25.

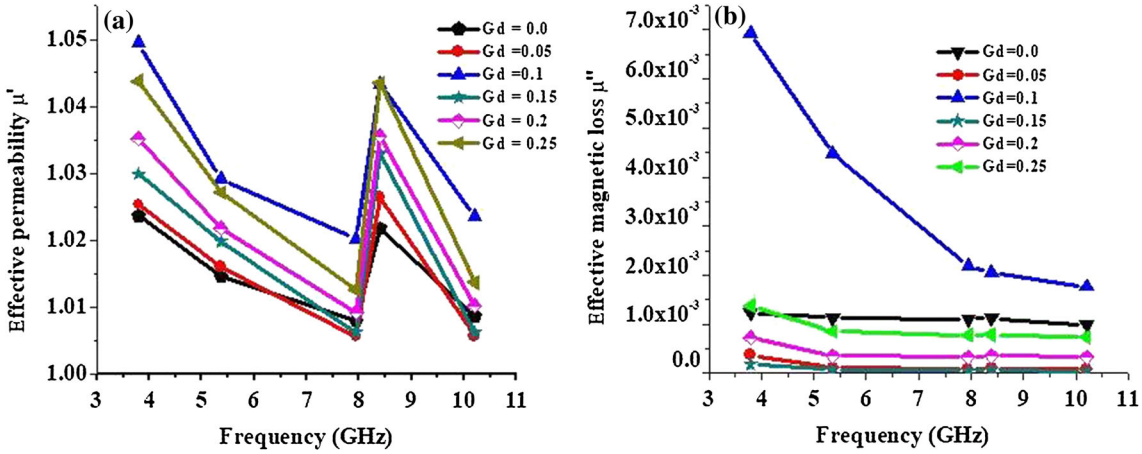

Fig. 8. Effective microwave complex permeability of the Gd-doped hexaferrite samples using the cavity perturbation method. (a) The effective permeability and (b) the effective magnetic loss. Magnetic permeability is close to 1 for all samples while magnetic losses are large when the Gd doping concentration is 0.10.

$$f = \frac{\gamma H_a}{2\pi}$$

where γ is the gyromagnetic ratio and H_a is the magnetocrystalline energy.[19]

From Fig. 8, the magnetic permeability is approximately 1 and the losses approach zero, implying that the ferromagnetic frequency is much lower than the measured frequency range. The overall effect of Gd doping has little effect on the microwave magnetic properties though a small increase in both the real and imaginary parts is noticed at Gd = 0.1%. The ferromagnetic resonance frequencies for Ba M-type hexagonal ferrites generally lie in the 30–40-GHz range; however, this is not noticed for this material.[3,8,31] The reason for these low values may be due to the large concentration of the impurities, which do not have large microwave permeability.[57]

CONCLUSIONS

This paper presents the structural, magnetic and microwave properties of Gd-doped Ca-Ba M-type hexaferrites. While the initial aim of this study was to obtain $Ca_{0.5}Ba_{0.5}Gd_xFe_{12-x}O_{19}$ (where x = 0…0.25), the results show that Gd may only substitute into the Ca-Ba M-type hexaferrite lattice at low initial doping concentrations (Gd < 0.1) with some formation of α-Fe_2O_3. At higher concentrations, the addition of Gd forces two noticeable secondary phases to be formed, α-Fe_2O_3 and $GdFeO_3$. While full substitution is not achieved, the presence of these phases has a large effect on the M–H loops obtained using a VSM. The microwave properties of the ferrite are largely unaffected by the Gd doping concentration, implying that the partially Gd-substituted Ca-Ba M-type hexaferrite has a similar low microwave permittivity and permeability to α-Fe_2O_3 and $GdFeO_3$.

ACKNOWLEDGEMENTS

One of the authors, Muddassara Kanwal, is thankful to the HEC, Pakistan for providing financial assistance under the IRSIP program to work in Cardiff Univ., UK, and also to Dr. Misbah-ul-Islam, Department of Physics, BZ University, Multan, Pakistan, and Dr. Mukhtar Ahmad, CIIT Lahore, Pakistan, for their valuable discussion on the manuscript.

REFERENCES

1. K.K. Mallick, P. Shepherd, and R.J. Green, *J. Eur. Ceram. Soc.* 27, 2045 (2007).
2. H. Pfeiffer, R.W. Chantrell, P. Görnert, W. Schüppel, E. Sinn, and M. Rösler, *J. Magn. Magn. Mater.* 125, 373 (1993).
3. J. Smit and H.P.J. Wijn, *Ferrites* (Eindhoven: Philips Technical Library, 1959).
4. W. Büchner, *Industrial Inorganic Chemistry* (London: VCH, 1989).
5. J. Qiu, M. Gu, and H. Shen, *J. Magn. Magn. Mater.* 295, 263 (2005).
6. Y.W. Dou, *Ferrite* (Nanjing: Jiangsu Science and Technology Press, 1996).
7. N. Dishovski, A. Petkov, I. Nedkov, and I. Razkazov, *IEEE Trans. Magn.* 30, 969 (1994).
8. R.C. Pullar, *Prog. Mater. Sci.* 57, 1191 (2012).
9. G. Albanese, *J. Phys. Colloq.* 38, C1-85 (1977).
10. J. Töpfer, S. Schwarzer, S. Senz, and D. Hesse, *J. Eur. Cerm. Soc.* 25, 1681 (2005).
11. F.M.M. Pereira, C. Junior, M.R.P. Santos, R.S.T.M. Sohn, F.N.A. Freire, J.M. Sasaki, J. De Paiva, and A.S.B. Sombra, *J. Mater. Sci. Mater. Electron.* 19, 627 (2008).
12. M.N. Ashiq, R.B. Qureshi, M.A. Malana, and M.F. Ehsan, *J. Alloys Compd.* 617, 437 (2014).
13. S. Sanghi and A. Agarwal, *J. Alloys Compd.* 513, 436 (2012).
14. A. Hooda, S. Sanghi, A. Agarwal, and R. Dahiya, *J. Magn. Magn. Mater.* 387, 46 (2015).
15. J.R. Morber, *One-dimensional Nanowires: Understanding Growth and Properties as Steps Toward Biomedical and Electrical Application* (Atlanta: Georgia Institute of Technology, 2008).
16. G. Dedigamua, P. Mukherjee, H. Srikanth, and S. Witanachchi, *Progress in Nanotechnology: Processing* (London: Wiley, 2010), p. 169.

17. I. Harward, R.E. Camley, and Z. Celinski, *Appl. Phys. Lett.* 105, 17 (2014).
18. A.M. Blanco and C. Gonzalez, *J. Phys. D Appl. Phys.* 24, 612 (1991).
19. S. Chang, S. Kangning, and C. Pengfei, *J. Magn. Magn. Mater.* 324, 802 (2012).
20. G. Litsardakis, I. Manolakis, and K. Efthimiadis, *J. Alloys Compd.* 427, 194 (2007).
21. G. Litsardakis, I. Manolakis, C. Serletis, and K. Efthimiadis, *J. Appl. Phys.* 103, 07E501 (2008).
22. G. Litsardakis, I. Manolakis, C. Serletis, and K. Efthimiadis, *J. Magn. Magn. Mater.* 316, 170 (2007).
23. F. Berry, J. Marco, C. Ponton, and K. Whittle, *J. Mat. Sci. Lett.* 20, 431 (2001).
24. M. Jamalian, A. Ghasemi, and M.J. Pourhosseini Asl, *J. Electron. Mater.* 44, 2856 (2015).
25. B. Rai, S. Mishra, V. Nguyen, and J. Liu, *J. Alloys Compd.* 581, 275 (2013).
26. G. Albanese, B. Watts, F. Leccabue, and S.D.A. Castañón, *J. Magn. Magn. Mater.* 184, 337 (1998).
27. F. Kools, A. Morel, R. Grössinger, J. Le Breton, and P. Tenaud, *J. Magn. Magn. Mater.* 242, 1270 (2002).
28. R. Grossinger, C. Tellez Blanco, M. Kupferling, M. Muller, and G. Wiesinger, *Phys. B* 327, 202 (2003).
29. J.S. McCloy, K. Korolev, J.V. Crum, and M.N. Afsar, *IEEE Trans. Magn.* 49, 546 (2013).
30. C.-J. Li, B. Wang, and J.-N. Wang, *J. Magn. Magn. Mater.* 324, 1305 (2012).
31. Z. Haijun, L. Zhichao, M. Chengliang, Y. Xi, Z. Liangying, and W. Mingzhong, *Mat. Sci. Eng. B* 96, 289 (2002).
32. J. Jia, C. Liu, N. Ma, G. Han, W. Weng, and P. Du, *Sci. Technol. Adv. Mater.* 14, 045002 (2013).
33. L. Chao and M.N. Afsar, *JApp. Phys.* 113, 17 (2013).
34. Ü. Özgüri, Y. Alivov, and H. Morkoç, Microwave ferrites, part 1: fundamental properties. *J. Mater. Sci. Mater. Electron.* 20, 789 (2009).
35. Y. Chen, A.L. Geiler, T. Chen, T. Sakai, C. Vittoria, and V.G. Harris, *J. Appl. Phys.* 101, 09M501 (2007).
36. J.A. Cuenca, S. Klein, R. Rüger, and A. Porch, in *44th European Microwave Conference (EuMC)*, p. 128 (2014).
37. J.A. Cuenca, E. Thomas, S. Mandal, O. Williams, and A. Porch, *IEEE Trans. Microw. Theory Tech.* 63, 4110 (2015).
38. D. Slocombe, A. Porch, E. Bustarret, and O.A. Williams, *Appl. Phys. Lett.* 102, 244102 (2013).
39. J.A. Cuenca, K. Bugler, S. Taylor, D. Morgan, P. Williams, J. Bauer, and A. Porch, *J. Phys. Condens. Matter* 28, 10 (2016).
40. L. Lechevallier, J.M.L. Breton, A. Morel, and P. Tenaud, *J. Phys. Condens. Matter* 20, 175203 (2008).
41. A. Deschamps and F. Bertaut, *CR Acad. Sci.* 17, 3069 (1957).
42. I. Ali, M. Islam, M. Awan, and M. Ahmad, *J. Electron. Mater.* 43, 512 (2014).
43. Y. Yang and X. Liu, *IEEE Trans. Magn.* 50, 1 (2014).
44. O. Hemeda, M. Said, and M. Barakat, *J. Magn. Magn. Mater.* 224, 132 (2001).
45. A. Ul-Haq and M. Anis-ur-Rehman, *Key Eng. Mat. Trans. Tech. Publ.* 510, 448 (2012).
46. P.E. Lippens, J.C. Jumas, and J.M. Génin, *ICAME 2005, France*, Vol. 1 (Berlin: Springer, 2007).
47. J. Park, Y.K. Hong, W. Lee, S.Y. An, J.W. Seo, and K.H. Hur, *IEEE Magn. Lett.* 6, 5500203 (2015).
48. S.H. Mahmood, A. Awadallah, Y. Maswadeh, and I. Bsoul, *IOP Conf. Ser.: Mater. Sci. Eng.* 92, 012008 (2015). https://doi.org/10.1088/1757-899X/92/1/012008.
49. B.D. Cullity and C.D. Graham, *Introduction to Magnetic Materials* (London: Wiley, 2011).
50. X. Batlle, X. Obradors, J. Rodríguez-Carvajal, M. Pernet, M. Cabanas, and M. Vallet, *J. Appl. Phys.* 70, 1614 (1991).
51. M. Han, Y. Ou, W. Chen, and L. Deng, *J. Alloys Compd.* 474, 185 (2009).
52. X. Liu, W. Zhong, S. Yang, Z. Yu, B. Gu, and Y. Du, *J. Magn. Magn. Mater.* 238, 207 (2002).
53. S. Ounnunkad, P. Winotai, and S. Phanichphant, *J. Electroceramics* 16, 357 (2006).
54. B. Balasubramanian, P. Mukherjee, R. Skomski, P. Manchanda, B. Das, and D.J. Sellmyer, *Sci. Rep.* 4, 6265 (2014).
55. F. Kools, *J. Phys. Colloq.* 46, C6-349 (1985).
56. R.M. Cornell and U. Schwertmann, *The Iron Oxides* (London: Wiley, 2006).
57. C.L. He, S.J. Ma, X.J. Su, Q.H. Mo, and J.L. Yang, *JMPEE* 49, 131 (2015).
58. S. Sahoo, P.K. Mahapatra, R.N.P. Choudhary, M.L. Nandagoswami, and A. Kumar, *Mater. Res. Express* 3, 065017 (2016).
59. C. Doroftei, E. Rezlescu, P. Dorin Popa, and N. Rezlescu, *Cryst. Res. Technol.* 41, 1112 (2006).
60. J.J. Thomson and J.C. Maxwell, *A Treatise on Electricity and Magnetism*, Vol. 2 (Charleston: BiblioLife, 2015).
61. K.W. Wagner, *Anna Phys.* 345, 817 (1913).
62. C. Koops, *Phys. Rev.* 83, 121 (1951).